

BIOCHEMISTRY

Simultaneous Fe²⁺/Fe³⁺ imaging shows Fe³⁺ over Fe²⁺ enrichment in Alzheimer's disease mouse brain

Yuting Wu^{1,2+}, Seyed-Fakhreddin Torabi³⁺, Ryan J. Lake¹⁺, Shanni Hong¹, Zhengxin Yu¹, Peiwen Wu³, Zhenglin Yang^{2,3}, Kevin Nelson³, Weijie Guo^{3,4}, Gregory T. Pawel¹, Jacqueline Van Stappen², Xiangli Shao^{1,2}, Liviu M. Mirica¹, Yi Lu^{1,2,3,4*}

Visualizing redox-active metal ions, such as Fe²⁺ and Fe³⁺ ions, are essential for understanding their roles in biological processes and human diseases. Despite the development of imaging probes and techniques, imaging both Fe²⁺ and Fe³⁺ simultaneously in living cells with high selectivity and sensitivity has not been reported. Here, we selected and developed DNAzyme-based fluorescent turn-on sensors that are selective for either Fe²⁺ or Fe³⁺, revealing a decreased Fe³⁺/Fe²⁺ ratio during ferroptosis and an increased Fe³⁺/Fe²⁺ ratio in Alzheimer's disease mouse brain. The elevated Fe³⁺/Fe²⁺ ratio was mainly observed in amyloid plaque regions, suggesting a correlation between amyloid plaques and the accumulation of Fe³⁺ and/or conversion of Fe²⁺ to Fe³⁺. Our sensors can provide deep insights into the biological roles of labile iron redox cycling.

INTRODUCTION

Redox-active metal ions play key roles in many biological processes such as oxygen transport, energy production, and oxidative stress-related neurodegenerative diseases (1, 2). A primary example is iron (Fe), which is mostly present in ferrous [Fe(II)/Fe²⁺] or ferric [Fe(III)/Fe³⁺] states in living organisms (3, 4). Dyshomeostasis of iron and its abnormal redox cycling can lead to ferroptosis, an iron-dependent programmed cell death pathway, which is a key process in many neurodegenerative diseases including Alzheimer's disease (AD) (5–9). In addition, ferroptosis has emerged as a promising therapeutic approach to cancers (10, 11). However, how redox equilibrium and dynamic speciation are involved in ferroptosis and related to AD or cancer remains poorly understood, partly because of a lack of highly selective sensors that allow for simultaneous monitoring of both Fe²⁺ and Fe³⁺. Such sensors require detection of either Fe²⁺ or Fe³⁺ without cross-reactivity with the opposite Fe oxidation state. Because of the chemical and physical similarities between these oxidation states, it has been quite challenging to develop sensors to detect both Fe²⁺ and Fe³⁺ simultaneously with high selectivity and sensitivity.

To achieve sensing of different redox states of iron, various methods have been explored but with limited success either in living cells or in vivo. For example, laboratory techniques, such as inductively coupled plasma mass spectrometry (12, 13), electron paramagnetic resonance (14), x-ray fluorescence (15), and magnetic resonance imaging (MRI) (16–18) have been developed but cannot readily provide spatial or temporal information in vivo because of their restrictive requirements for sample pretreatment or excessive time needed for data collection. It has been shown that “labile” iron pools, which comprise only a small portion of total iron, play critical roles in many cellular processes, including lipid oxidation during

ferroptosis and generating free radicals in AD (19–21), and all of the above methods can measure only the total iron without differentiating labile iron pools. To visualize these labile iron pools, histochemical methods based on potassium ferricyanide or potassium ferrocyanide was developed to distinguish Fe²⁺ from Fe³⁺ and acquire spatial information (22), but this method can only detect Fe²⁺ or Fe³⁺ separately on fixed tissue slices, not in living cells or in vivo, because the detection is based on forming insoluble blue pigments. In addition, ferricyanide can react with many other metal ions, such as Zn²⁺ and Cu²⁺, and thus is vulnerable to interference from these metal ions.

Fluorescence sensors have also been developed to visualize labile Fe²⁺ and Fe³⁺ simultaneously in vivo and provide spatiotemporal information in living cells. However, most of these methods either have low selectivity for Fe²⁺ and Fe³⁺ over other metal ions, require organic solvents, or cannot be adapted readily for in vivo sensing applications. Recently, some Fe²⁺ sensors based on organic molecules and fluorophores have achieved sufficient selectivity and sensitivity for imaging in cells (23–26) and in mouse models (27, 28). To image two different oxidation states of the same metal ions, such as Fe²⁺ and Fe³⁺ simultaneously, we need two sensors that are not only specific for the respective Fe²⁺ or Fe³⁺ but also two fluorophores that do not have much overlapping excitation and emission spectra to avoid interference in the detection. Because the target recognition and fluorescent readouts of the organic molecule sensors are coupled together, it is difficult to replace the fluorophore with one that has a different fluorescence emission spectrum to avoid overlap of fluorescent signals. Changing fluorophore moieties for these sensors normally requires redesign of the sensors, which can adversely affect their other properties, such as loss of brightness of fluorescence, reduced selectivity, or change of subcellular localization of the sensor (29). Therefore, to the best of our knowledge, the simultaneous monitoring of two oxidation states of the same metal ion in living cells or in vivo has not yet been reported. As a result, the redox equilibrium and dynamic distribution of Fe²⁺ and Fe³⁺ have not been investigated, although they have been hypothesized to play important roles on many

¹Department of Chemistry, University of Illinois at Urbana-Champaign, Urbana, IL 61801, USA. ²Department of Chemistry, University of Texas at Austin, Austin, TX 78712, USA. ³Department of Biochemistry, University of Illinois at Urbana-Champaign, Urbana, IL 61801, USA. ⁴Department of Molecular Bioscience, University of Texas at Austin, Austin, TX 78712, USA.

[†]These authors contributed equally to this work.

*Corresponding author. Email: yi.lu@utexas.edu

Copyright © 2023
The Authors, some
rights reserved;
exclusive licensee
American Association
for the Advancement
of Science. No claim to
original U.S. Government
Works. Distributed
under a Creative
Commons Attribution
License 4.0 (CC BY).

Downloaded from https://www.science.org at University of Illinois - Urbana on February 27, 2025

biological processes including ferroptosis in neurodegenerative diseases such as AD.

To overcome the technical barrier for simultaneous monitoring Fe^{2+} and Fe^{3+} in vivo and to fill a major knowledge gap of redox equilibrium, dynamic distribution of $\text{Fe}^{2+}/\text{Fe}^{3+}$, and their roles in neurodegenerative diseases, we take advantage of DNAzyme-based "catalytic beacon" sensors. DNAzymes, also called deoxyribozymes, are DNA molecules that display enzymatic activities, such as protein enzymes and ribozymes, in the presence of a cofactor such as metal ions (30–36). DNAzymes are typically isolated from a large DNA library of up to 10^{15} different sequences through a combinatorial process called in vitro selection (37). Among them, RNA-cleaving DNAzymes are of particular interest for sensing metal ions because these DNAzymes are often specific for a certain metal ion cofactor (30, 32). By conjugating a fluorophore at the end of the enzyme strand, two quenchers at the opposite termini of the enzyme strand and complementary substrate strand, respectively, we take the advantage of melting temperature differences before and after DNAzyme-catalyzed cleavage of the substrate strand and have developed a catalytic beacon approach (38–48) that produces metal ion-specific fluorescent turn-on sensors (Fig. 1, A and B). Because the fluorophore is physically separated from the metal-binding site and fluorescent signal arises from the release of the fluorophore-labeled substrate upon cleavage, this approach can be used to sense metal ions using any fluorophore. Therefore, it is possible to use DNAzyme beacons labeled with different fluorophores that have distinct emission wavelengths for simultaneous monitoring of two or more targets. Through efforts from many laboratories, including our laboratory, DNAzymes highly selective for different metal ions have been obtained, including Cr^{3+} (49), Ca^{2+} (50), Cd^{2+} (51), Co^{2+} (52), Cu^{2+} (53), Mg^{2+} (54), Pb^{2+} (30), UO_2^{2+} (40), Zn^{2+} (32, 55, 56), Ag^+ (57), Li^+ (58), and Na^+ (59, 60). Despite decades of success using this approach, no in cellulo or in vivo DNAzyme sensor that can differentiate different oxidation states of the same metal ion has been reported.

In this study, we report in vitro selection and development of DNAzyme sensors with high specificity for either Fe^{2+} or Fe^{3+} , which allows us to visualize both Fe^{2+} and Fe^{3+} simultaneously in living cells and brain slices of AD mice models. Correlated signal changes were observed with the regulation of iron levels by addition of transferrin (Tf), an iron transport protein (61), or deferoxamine (DFO), an iron chelator (62). We further apply these sensors to detect iron changes during ferroptosis in living cells and observed a decrease of $\text{Fe}^{3+}/\text{Fe}^{2+}$ redox ratio over time, which suggests that iron is a potential source related to the oxidative stress accumulation in this cell death pathway (7). The sensors provided spatial distributions of Fe^{2+} and Fe^{3+} , as well as iron redox ratios, revealing a statistically significant increase in the $\text{Fe}^{3+}/\text{Fe}^{2+}$ ratio surrounding amyloid plaque regions but not in other brain regions and suggesting that not only total iron but also iron redox cycling play a key role in the progression of AD. These finding also suggests a correlation between amyloid plaques and the accumulation of Fe^{3+} and/or the conversion from Fe^{2+} into Fe^{3+} , which provides potential direction for further functional study to understand metal redox in AD progression. These results demonstrate that simultaneous monitoring of Fe^{2+} and Fe^{3+} using iron-specific DNAzyme-based sensors provides deeper insight into the roles of redox cycling of labile iron in neurodegenerative diseases.

RESULTS

In vitro selection of Fe^{2+} and Fe^{3+} -specific DNAzymes

To obtain Fe^{2+} -specific DNAzymes, in vitro selection was conducted in an anaerobic glove box because Fe^{2+} is readily oxidized to Fe^{3+} in the presence of oxygen (fig. S1). Parallel selections were carried out in the presence or absence of 1 mM glutathione, a highly abundant cytosolic metabolite predicted to form a complex with Fe^{2+} intracellularly (63). A negative selection against the selection buffer without Fe^{2+} was incorporated before the first round, and counter selections against Mn^{2+} , Co^{2+} , Zn^{2+} , Cd^{2+} , and Pb^{2+} were introduced starting from the third round of the selections to remove DNAzymes that catalyzed the cleavage of the substrate in the presence of other components in the selection buffer or other divalent metal ions. These additional steps were necessary to improve the selectivity of the isolated DNAzymes (fig. S2) (59). The selection was monitored by measuring the percent cleavage activity in the presence of Fe^{2+} in each round and was continued for nine rounds (fig. S3). Enrichment of highly Fe^{2+} -specific DNAzymes and effectiveness of counter selection was confirmed by evaluating cleavage activity of the selected pools in the presence of Fe^{2+} or Fe^{3+} or several other divalent metal ions (figs. S4 and S5). From cloning and sequencing, a total of 149 sequences were identified from different conditions (figs. S6 to S9 and table S1). Upon testing representative individual sequences for their Fe^{2+} -dependent activity, the most active and selective sequence (fig. S10), named Fe(II)-H5, was chosen for sensor development. First, on the basis of the predicted secondary structures of the Fe(II)-H5 cis-acting DNAzyme, we generated six trans-acting DNAzymes consisting of a separate enzyme (E) and substrate (S) strands by truncating sequences at different sites and testing their cleavage activity (fig. S11). The truncation studies resulted in an active trans-cleaving DNAzyme with minimal catalytic sequence (truncation-2b in fig. S11). Such a trans-cleaving DNAzyme is suitable for conjugating to fluorophore and quenchers and compatible with the catalytic beacon sensing strategy (Fig. 1A).

With the goal of selecting Fe^{3+} -specific DNAzymes, several in vitro selection conditions and strategies were tested. We found that the choice of in vitro selection condition including components to solubilize Fe^{3+} while keeping it accessible to the DNA molecules in the initial library is critical to the successful isolation of Fe^{3+} -specific DNAzymes. As a result of these tests, in vitro selection was conducted in the presence of 5 mM bis-tris in an acetate buffer at pH 5.5, which we found was able to stabilize Fe^{3+} in a soluble form (fig. S12) because Fe^{3+} is known to readily form insoluble iron hydroxide complexes at pH > 2.6 if not stabilized with a weakly chelating agent such as bis-tris (fig. S13). Inclusion of strong chelators such as citrate ions that can solubilize Fe^{3+} resulted in failure in isolating Fe^{3+} -specific DNAzymes, perhaps because of the inability of DNA molecules to compete with such chelators in binding to Fe^{3+} . Negative selections against the same buffer without Fe^{3+} were incorporated starting from round 1 before each positive selection to decrease the chance of isolating Fe^{3+} -independent DNAzymes. The in vitro selection process was continued until the ratio of Fe^{3+} -specific activity over background cleavage started to drop after round 9 (fig. S14). The enriched pools did not show substantial cleavage activity in the presence of several other metal ions at 50 μM , such as Fe^{2+} , Mg^{2+} , Ca^{2+} , Sr^{2+} , Ba^{2+} , Mn^{2+} , Co^{2+} , Ni^{2+} , Cu^{2+} , Zn^{2+} , Cd^{2+} , Pb^{2+} , Eu^{3+} , Sm^{3+} , In^{3+} , Tb^{3+} , and Yb^{3+} (fig.

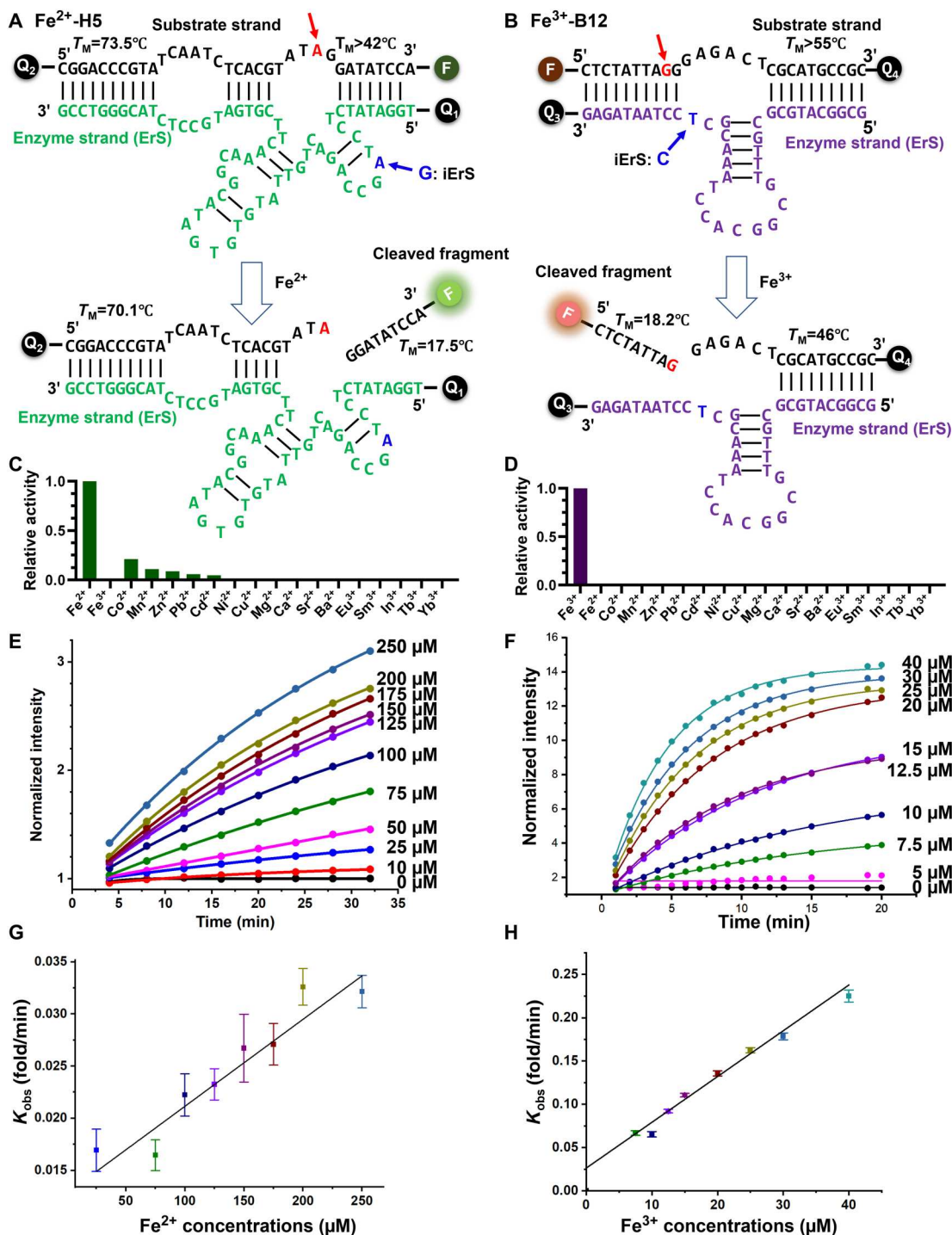


Fig. 1. The sequences of the Fe^{2+} - and Fe^{3+} -specific DNAzymes and the design, sensitivity, and selectivity of their fluorescent sensors. (A) Secondary structure of the trans-cleaving Fe^{2+} -specific DNAzyme [Fe(II)-H5], consisting of an enzyme strand shown in green with a lowa Black FQ quencher (Q1) at the 5' end, and a substrate strand shown in black with the same quencher (Q2) at the 5' end and an Alexa Fluor 488 fluorophore (F1) at the 3' end. (B) Secondary structure of the trans-cleaving Fe^{3+} -specific DNAzyme [Fe(III)-B12], consisting of an enzyme strand shown in purple with a lowa Black RQ quencher (Q3) at the 3' end, and a substrate strand shown in black with a 5' Alexa Fluor 647 fluorophore (F2) and a second lowa Black RQ quencher (Q4) at the 3' end. Both DNAzymes contain a ribonucleotide cleavage site (red, arrow). In addition, a mutation in the enzyme strand shown in blue [A to G in the Fe(II)-H5 DNAzyme and T to C in the Fe(III)-B12 DNAzyme] rendered the respective DNAzymes inactive and thus served as negative controls. (C and D) Selectivity of the trans-cleaving Fe(II)-H5 (C) and Fe(III)-B12 (D) DNAzymes. Fraction of the cleaved substrate in the presence of different metal ions in 20 mM acetate buffer (pH 6.0), 5 mM bis-tris, and 200 mM NaCl analyzed via denaturing polyacrylamide gel electrophoresis (PAGE). (E and F) Normalized fluorescence intensity of the Fe(II)-H5 DNAzyme (E) and the Fe(III)-B12 DNAzyme (F) sensors in response to different concentrations of Fe^{2+} or Fe^{3+} , respectively. (G and H) The initial fluorescence turn-on rates (k_{obs}) of the sensors at different iron concentrations are shown in (G) for the Fe(II)-H5 DNAzyme and in (H) for the Fe(III)-B12 DNAzyme.

S15). From cloning and sequencing, a total of 157 DNazymes were isolated from different selection conditions (table S2). The resulting sequences were aligned on the basis of their primary sequence similarities (figs. S16 to S19). The activity of several representative DNazymes were tested, and one of the most active DNazymes, called Fe(III)-B12 (fig. S20), was converted into trans-cleaving DNazymes, by truncation studies. The truncation study was based on predicted secondary structures of the cis-acting Fe(III)-B12 DNzyme (fig. S21). The cleavage activities of three trans-acting DNazymes generated by truncating B12 sequence at different sites were tested. The secondary structure of trans-acting Fe(III)-B12 DNzyme with minimal catalytic region (fig. S21) was used to design the Fe³⁺-dependent DNzyme-based fluorescent sensor (Fig. 1B). To confirm the selectivity of the trans-cleaving iron DNazymes, we evaluated the cleavage activity of the Fe(II)-H5 and Fe(III)-B12 DNazymes in the presence of different metal ions at 100 μM including Fe²⁺, Fe³⁺, Co²⁺, Mn²⁺, Zn²⁺, Pb²⁺, Cd²⁺, Ni²⁺, Cu²⁺, Mg²⁺, Ca²⁺, Sr²⁺, Ba²⁺, Eu³⁺, Sm³⁺, In³⁺, Tb³⁺, and Yb³⁺. Both DNazymes exhibit excellent selectivity for their respective iron oxidation state (Fig. 1, C and D).

Conversion and characterization of fluorescent DNzyme sensors

To convert the Fe²⁺- and Fe³⁺-specific DNazymes into fluorescent sensors, we applied the catalytic beacon design (Fig. 1, A and B) by incorporating a fluorophore (F) on one end of the substrate strand and an intermolecular quencher (Q1 or Q3) on opposite termini of the enzyme strand. The enzyme strand can bind to the substrate strand through DNA-DNA hybridization of the two binding arms. In addition, the substrate strand, which contains a ribonucleotide cleavage site, is labeled with an intramolecular quencher (Q2 or Q4) to suppress background fluorescence without substrate strand being cleaved (39). The binding arms are designed to be long enough that the melting temperature of the entire complex is higher than the desired ambient temperature (e.g., 37°C for cellular studies). Therefore, the enzyme and uncleaved substrate strands can stably hybridize to each other under assay conditions. Upon metal-induced cleavage of the substrate at the internal ribonucleotide site, the resulting fluorophore-labeled fragment has a much lower melting temperature (<20°C). This decrease in melting temperature allows the fluorophore-labeled fragment to dissociate from the complex, resulting in the release of the fluorophore from both inter- and intramolecular quenchers, followed by a substantial increase in fluorescent signal. Because this design decouples the fluorophores from metal-dependent DNzyme-based cleavage of the substrate, any fluorophore and quencher pairs can be readily adapted to the sensors to achieve sensing with different excitation and emission wavelengths. Moreover, both Fe²⁺ and Fe³⁺ are known to quench fluorescence of fluorophores nonspecifically. Separating the Fe²⁺- and Fe³⁺-binding site away from the fluorophore helps minimize this issue, allowing to build Fe²⁺- and Fe³⁺-specific DNzyme sensors with turn-on signals.

Taking advantage of the above design, we incorporated Alexa Fluor 488 in the Fe²⁺-selective DNzyme [Fe(II)-H5] and Alexa Fluor 647 in the Fe³⁺-selective DNzyme [Fe(III)-B12] for simultaneous detection of both oxidation states of iron using two different fluorescent channels. Furthermore, to eliminate the artifact of fluorescent signals due to anything other than Fe²⁺- and Fe³⁺-specific activity of the DNazymes (e.g., sensor degradation under

intracellular conditions), inactive DNazymes (iERs) that contain single-nucleotide mutations that abolish DNzyme cleavage activity [labeled in blue in Fig. 1 (A and B)] were used. Increase in the fluorescent signal of the Fe(II)-H5 (Fig. 1E) and the Fe(III)-B12 (Fig. 1F) DNzyme sensors were measured in the presence of different concentrations of Fe²⁺ or Fe³⁺, respectively. Both sensors showed linear signal increase in response to increasing concentrations of their respective metal ions in a physiologically relevant range (Fig. 1, G and H, and fig. S22). In addition, our DNzyme-based sensors show excellent selectivity for their cognate metal ion target over the different oxidation state of the same metal ion, as well as other biologically relevant metal ions (figs. S23 and S24).

DNzyme sensors monitor Fe²⁺ and Fe³⁺ simultaneously in living cells

Having demonstrated high selectivity for either Fe²⁺ or Fe³⁺ by our DNzyme sensors under physiologically relevant concentrations, we explored imaging Fe²⁺ and Fe³⁺ in the endosomal-lysosomal system within living cells. This system is the entry point of the iron transport protein, Tf, which is the major iron import pathway in mammalian cells by binding to and importing extracellular Fe³⁺. In addition, the endosomal-lysosomal system is known to contain both Fe²⁺ and Fe³⁺ labile pools due to the presence of metalloredox enzymes such as six-transmembrane epithelial antigen of the prostate 3 (Metalloredox STEAP3), which reduces Fe³⁺ to Fe²⁺, thus enabling its further transport into the cytosol (64, 65). To deliver the DNzyme sensors into the endosomal-lysosomal system, we used polyethylenimine (PEI), which has previously been used to deliver nanosensors into the endosomal-lysosomal system successfully (66–68). The colocalization of the signal from DNzyme sensors and LysoTracker Red, a lysosome marker (69), confirms efficient delivery of our sensors into lysosomes of the cells (Fig. 2A and fig. S25). The Pearson's correlation coefficient between the iron pools and LysoTracker was around 50 to 60% (table S3), suggesting that although most of the iron signal was localized in lysosome, it was not evenly distributed, as not all the LysoTracker-positive regions showed iron signals. It is also possible that a small portion of Fe²⁺ or Fe³⁺ may be present in other parts of the cells. To introduce different iron concentrations in endo-lysosomes, the cells were incubated in an iron-deficient medium with increasing concentrations of Tf (61) or with DFO as an iron chelator to decrease the level of labile iron (62). Both the Fe(II)-H5 and Fe(III)-B12 DNzyme sensors showed increase in fluorescent signal within lysosomes in response to increasing concentrations of Tf (Fig. 2). This observation is expected even for Fe²⁺ because of the reduction of Fe³⁺ to Fe²⁺ by endogenous metalloredox enzymes in the endosomal-lysosomal system (64, 65). However, the increase in the 5 μM Tf group was only 1.9-fold for Fe²⁺ and 1.6-fold for Fe³⁺, which may be due to the limited iron source in iron-deficient medium. To support this explanation, cells were also incubated in normal cell media, and around 4-fold increase was observed for both Fe³⁺ and Fe²⁺. In contrast, treating cells with DFO resulted in a 5.7- to 5.8-fold decrease of iron, as indicated by both DNzyme sensors in iron-deficient media but only a 1.4- to 1.8-fold decrease of iron in normal media (Fig. 2 and figs. S26 to S28). Together, these results demonstrate that the Fe(II)-H5 and Fe(III)-B12 DNzyme sensors can be used to image labile Fe²⁺ and Fe³⁺ in endo-lysosomes simultaneously. To the best of our knowledge, this is the first time that simultaneous imaging of Fe²⁺

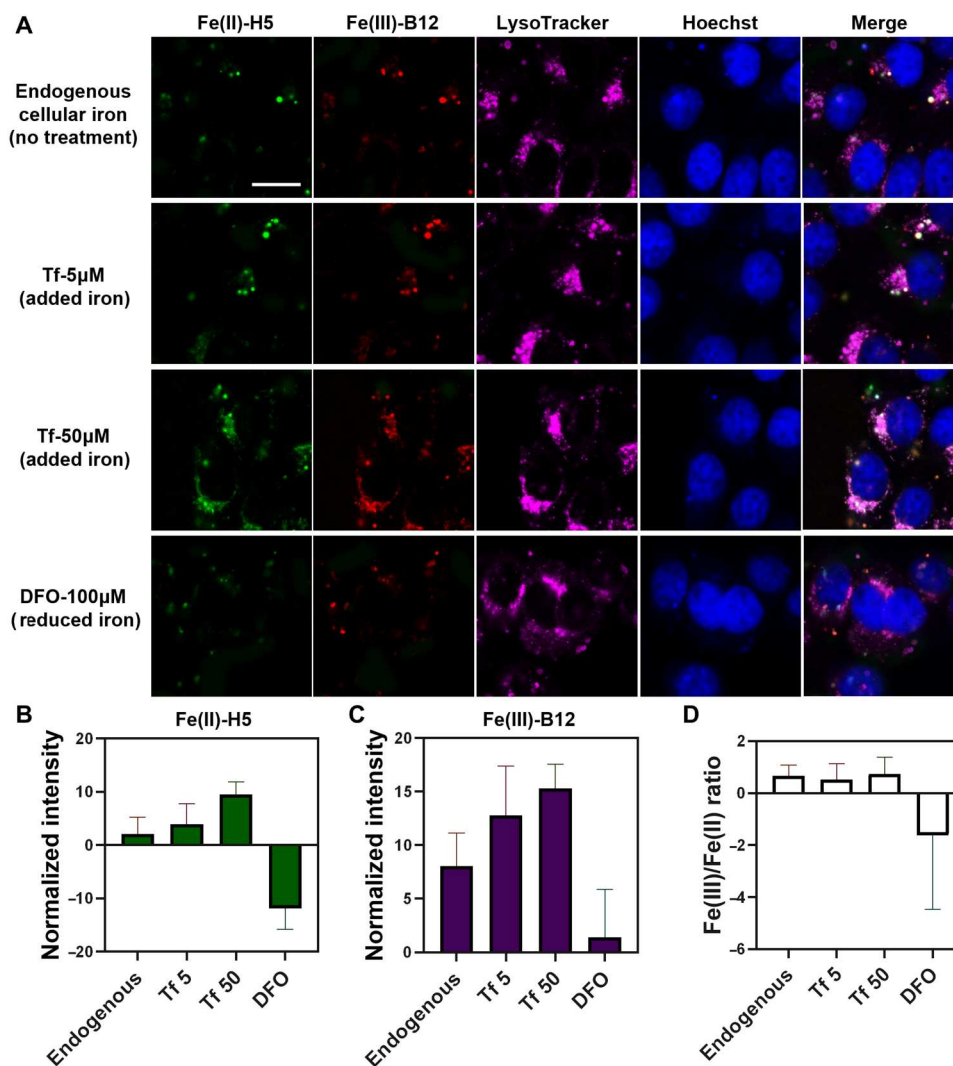


Fig. 2. Simultaneous imaging of labile Fe^{2+} and Fe^{3+} in HepG2 cells. (A) HepG2 cells transfected with the Fe(II)-H5 (green) and the Fe(III)-B12 (red) DNAzyme sensors using PEI. Lysosomes are stained with LysoTracker Red and are shown in magenta. Cells were without any additional treatment to image endogenous (endo) iron, treated with 5 or 50 μM Transferrin (Tf) to increase lysosomal iron, or with 100 μM iron chelator DFO to decrease intracellular iron. (B) Statistical analysis of mean fluorescence intensity in LysoTracker-labeled region in (A) reveals that Fe^{2+} increased 1.9-fold when treated with 5 μM Tf and increased 4.6-fold when treated with 50 μM Tf, while Fe^{2+} decreased to barely detectable when treated with 100 μM DFO. (C) Statistical analysis of mean fluorescence intensity in (A) reveal that Fe^{3+} increased 1.6-fold when treated with 5 μM Tf and increased 1.9-fold when treated with 50 μM Tf and decreased around 5.7-fold when treated with 100 μM DFO. Cells were cultured in iron-deficient medium during the treatments. Error bars represent SEMs of the LysoTracker-labeled region in 20 different cells in each sample. Fluorescence intensity was normalized with ErS-iErS. Scale bar, 20 μm . (D) The $\text{Fe}^{3+}/\text{Fe}^{2+}$ ratio was calculated based on the mean fluorescence intensity of Fe^{2+} (B) and Fe^{3+} (C) in the LysoTracker region. When comparing with endogenous $\text{Fe}^{3+}/\text{Fe}^{2+}$ ratio in cells that were in the iron deficient media, no significant change in the $\text{Fe}^{3+}/\text{Fe}^{2+}$ ratio was observed in cells that were treated with different concentrations of Tf, and a 2.4-fold decrease of the $\text{Fe}^{3+}/\text{Fe}^{2+}$ ratio was observed in cells that were treated with 100 μM DFO.

and Fe^{3+} within the same location of a live cell has been demonstrated.

To quantify iron redox changes using our sensors, we calculated the $\text{Fe}^{3+}/\text{Fe}^{2+}$ ratio when treating the cells with Tf or DFO. As shown in Fig. 2D, we observed no significant change of the $\text{Fe}^{3+}/\text{Fe}^{2+}$ ratio. This is probably because the Fe^{3+} imported by Tf is readily converted into Fe^{2+} because of the reducing environment inside the endosomal-lysosomal system (65). Moreover, when treating the cells with DFO, the $\text{Fe}^{3+}/\text{Fe}^{2+}$ ratio decreased 2.4-fold. This observation is consistent with previous report that DFO is a Fe^{3+} chelator (62), which can bind to Fe^{3+} and decrease its concentration.

The above results illustrated that Fe^{2+} and Fe^{3+} detection in an endo-lysosomal system is a result of guided delivery of the sensors using PEI. When we delivered the sensors using TurboFect, a delivery agent that has less subcellular localization effect, the sensor distributed more evenly inside of the cell and showed the presence of Fe^{2+} and Fe^{3+} in other parts of the cell, such as nucleus and cytoplasm (figs. S27 and S28). Thus, the delivery agents used for the sensors could influence the subcellular localization of the sensors. To calibrate our sensors with other iron sensors, we costained the Fe(II)-H5 DNAzyme sensor with FerroOrange, a commercially available Fe^{2+} sensor, and observed a similar increase in

fluorescence intensity when adding excess amounts of iron (100 μM ferric ammonium citrate; fig. S29). However, less change in fluorescence intensity was observed in the presence of the iron chelator DFO. This difference suggests that FerroOrange is probably less sensitive in the presence of low concentrations of iron. We also found that the pattern of FerroOrange was similar but not the same as the signal from our Fe^{2+} sensor (fig. S29). Specifically, both sensors showed similar fluorescence distribution in cytoplasm in general, but our sensors showed an increased intensity for some of the cytoplasm regions. In addition, our sensor detected iron signal in the nucleus, which was not the case for FerroOrange. These differences are expected, as each sensor has its own cellular delivery efficiency, subcellular localization preference, sensitivity, and selectivity toward Fe^{2+} . For example, FerroOrange was known to favor a localization in the Golgi and endoplasmic reticulum (70). To find out whether the difference in subcellular localization is responsible for the observed differences, we delivered the FerroOrange with PEI to help concentrate the sensor in the endosomal-lysosomal system and observed an enriched FerroOrange signal in the endosomal-lysosomal system (fig. S30). These results indicate that our sensor can show a similar trend as FerroOrange, yet it is more sensitive to iron.

Increase in both Fe^{3+} and Fe^{2+} levels but decrease in $\text{Fe}^{3+}/\text{Fe}^{2+}$ ratio in ferroptotic cells

Next, we investigated whether our DNAzyme-based sensors can detect changes in iron redox states by using the Fe(II)-H5 and Fe(III)-B12 sensors to monitor Fe^{2+} and Fe^{3+} and their conversion during ferroptosis, which can be triggered by lipid peroxidation related to excess amounts of iron and its resulting Fenton reaction (5, 71). To induce ferroptosis in our model system, we incubated HepG2 cells with RAS-selective lethal 3 (RSL3) (72, 73), which is a well-known ferroptosis inducer. RSL3 inhibits glutathione peroxidase 4 (GPX4), which eliminates phospholipid peroxides, and thus allows lipid peroxides to accumulate because of iron-mediated Fenton chemistry, triggering ferroptosis-induced cell death without directly modulating total iron levels (74). The 3-(4,5-dimethylthiazol-2-yl)-2,5-diphenyl-2*H*-tetrazolium bromide (MTT) assay (75) showed RSL3-induced cell death over 8 hours (fig. S31). By monitoring the cells in this 8-hour window of ferroptosis, we observed a rapid increase of both Fe^{2+} (Fig. 3, A and B, and figs. S32 and S33A) and Fe^{3+} (Fig. 3, A and C, and figs. S32 and S33B) levels in the LysoTracker-labeled region within the first 4 hours of ferroptosis. These results indicate a rapid generation of labile Fe^{2+} and Fe^{3+} within lysosomes during the initiation stage of the ferroptosis. We observed a larger increase of Fe^{2+} (2.3-fold increase from 0 to 2 hours and 4.3-fold increase from 2 to 4 hours) than that of Fe^{3+} (2.8-fold increase of from 0 to 4 hours). As a result, we observed a continuous decrease of the $\text{Fe}^{3+}/\text{Fe}^{2+}$ ratio during ferroptosis (Fig. 3D), which indicates that the reduction of Fe^{3+} to Fe^{2+} could serve as a source for labile Fe^{2+} in endo-lysosomes. After 4 hours, both iron levels decreased, indicating that, in the later stage of ferroptosis, the labile iron pools are being depleted from the endo-lysosome. These results demonstrate that simultaneous monitoring of Fe^{2+} and Fe^{3+} levels by our DNAzyme-based sensors can provide insights into unexplored roles of labile Fe^{2+} and Fe^{3+} during ferroptosis.

Elevated iron redox levels accumulate in amyloid β plaque regions in AD mouse brain

We next investigated the ability of our DNAzyme-based sensors to monitor labile iron levels in a more complicated biological model. Increasing evidence has linked ferroptosis to AD because elevated iron levels were also observed in AD patients' brains, and thus, excessive accumulation of iron is considered as a risk factor in the development of AD (76). However, limited information on spatial distribution of Fe^{2+} and Fe^{3+} and their redox dynamics in AD pathogenesis is available, partly because of the limitations of existing iron sensors. To address this unmet need, we further applied our sensors to image labile iron in brain slices of AD mice to gain insights into the relationship between iron redox activity and AD progression. Fe^{2+} and Fe^{3+} were detected simultaneously in the cortex region and compared between 11-month-old wild-type (WT) mice and 5xFAD mice that express mutant humanized amyloid precursor protein and mutant human presenilin 1 (PSEN1) transgenes, which are commonly used as an AD model (Fig. 4A) (77). A 2.3-fold increase in the Fe^{2+} level (Fig. 4B) and a 7.9-fold increase in the Fe^{3+} level (Fig. 4C) was observed in whole-brain slices from 5xFAD mice when compared to the WT controls, indicating that Fe^{3+} accumulates in the AD mouse brains more than Fe^{2+} . To understand the involvement of iron redox in the AD pathogenesis, we further investigated the distribution of iron oxidation states in relation to amyloid β ($\text{A}\beta$) formation, which accumulates in AD brain and contributes to neurotoxicity (77), by comparing the fluorescence intensity of our Fe^{2+} and Fe^{3+} DNAzyme-based sensors in the cortex regions that have either $\text{A}\beta$ plaques or not. Both iron sensors were co-stained with HJ3.4 antibody, which labels immunoreactive $\text{A}\beta$ plaques (78). Fe^{2+} was increased by 2.1-fold in and surrounding the cortex regions that have $\text{A}\beta$ plaque deposition [called $\text{A}\beta$ plaque deposition region (APDR)], while Fe^{2+} was elevated by 1.7-fold in the surrounding cortex regions that did not show $\text{A}\beta$ plaque deposition (called non-APDR; Fig. 4D). The statistical analysis showed that the increase in the level of Fe^{2+} in both APDR and non-APDR was significant when compared with the WT controls. However, there was no significant difference between APDR and non-APDR Fe^{2+} levels, which suggests a similar elevation of Fe^{2+} levels in the cortex regions of AD mouse. In contrast, we observed a 2.6-fold and an 8.7-fold increase in the levels of Fe^{3+} in non-APDR and APDR, respectively, when compared with their WT controls (Fig. 4E). These observations suggest that the accumulation of the oxidized state of iron in AD brain is preferentially enriched in APDR. Because of the nonhomogenous distribution, such a closer observation and analysis instead of a brief comparison on whole-brain slices is necessary to understand how iron redox correlates with AD models.

To understand the role of iron redox cycling in AD progression, we further used our sensors to compare the relative $\text{Fe}^{3+}/\text{Fe}^{2+}$ ratios based on the fluorescence difference between 5xFAD mice and WT mouse brains. When performing the comparison with whole-brain slices, we observed a 2.4-fold increase of $\text{Fe}^{3+}/\text{Fe}^{2+}$ ratio in AD mouse cortex when compared with its WT controls (Fig. 4F). We then analyzed the spatial information of these redox changes in detail and found a 1.6-fold increase in the relative $\text{Fe}^{3+}/\text{Fe}^{2+}$ ratio in non-APDR and a 3.1-fold elevation in the relative $\text{Fe}^{3+}/\text{Fe}^{2+}$ in APDR of 5xFAD mouse brains when compared with WT mouse brains (Fig. 4G). This observation reveals that oxidative stress in AD brains is associated with aggregation of $\text{A}\beta$. Although Fe^{3+}

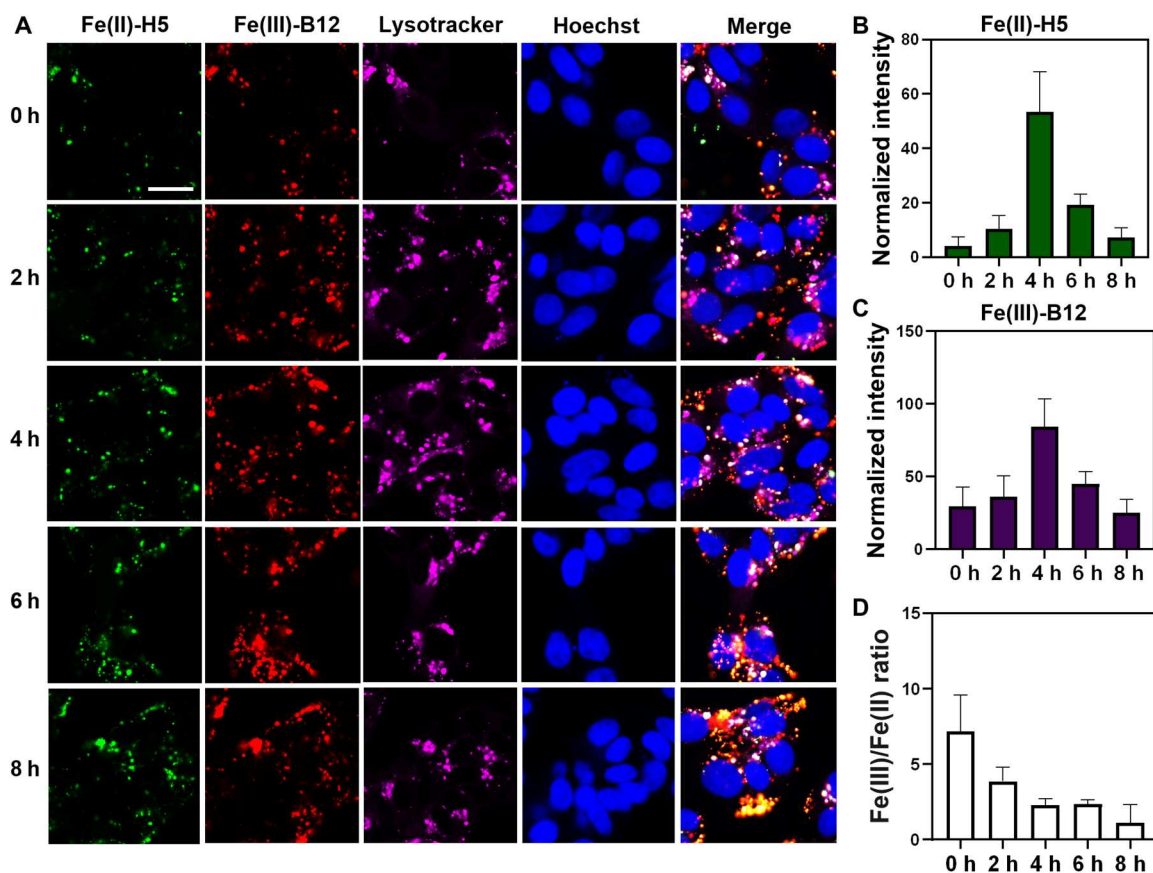


Fig. 3. Ferroptosis triggers an elevation in the intracellular Fe^{2+} and Fe^{3+} pools with a decreased $\text{Fe}^{3+}/\text{Fe}^{2+}$ ratio. (A) Fe(II)-H5 (green) and Fe(III)-B12 (red) DNAzyme sensors detecting labile pools of Fe^{2+} and Fe^{3+} simultaneously during RSL3-induced ferroptosis at different time points. LysoTracker Red and Hoechst 33258 were used to label lysosomes (magenta) and nucleus (blue), respectively. (B and C) Statistical analysis of normalized fluorescence intensity in the LysoTracker-labeled region reveals an increase of Fe^{2+} (B) and Fe^{3+} (C) within the first 4 hours and a decrease of Fe^{2+} and Fe^{3+} within 4 to 8 hours of RSL3-induced ferroptosis in the endosomal-lysosomal system. (D) The $\text{Fe}^{3+}/\text{Fe}^{2+}$ ratio decreases during ferroptosis. Scale bar, 20 μm . h, hours.

aggregates with $\text{A}\beta$ plaques and could reduce to Fe^{2+} to serve as one of the sources for generating reactive oxygen species (79–81), the $\text{Fe}^{3+}/\text{Fe}^{2+}$ level is still high around $\text{A}\beta$ plaque regions, suggesting the potential existence of a continuous source of Fe^{3+} diffusing out from surrounding cells and/or proteins, or a different mechanism of $\text{A}\beta$ plaque/ferric ion-related reactive oxygen species (ROS) generation. From these results, we have validated that both the Fe(II)-H5 and Fe(III)-B12 DNAzyme sensors can monitor the dynamic of Fe^{2+} and Fe^{3+} interconversion and provide spatiotemporal information that will gain deeper insights into iron-related diseases such as AD.

DISCUSSION

Visualizing different oxidation states of redox-active metals provides valuable information for understanding the role of metal redox in regulating biological processes and human health. Despite this importance, current imaging tools are limited, and simultaneous imaging of different oxidation states of the same metal ion has yet to have been reported. To overcome these limitations, we have isolated DNAzymes that are highly specific for either Fe^{2+} or Fe^{3+} through in vitro selection. Upon further characterization and conversion into fluorescent sensors using the catalytic beacon

strategy, we demonstrate the ability to use these DNAzyme-based turn-on fluorescent sensors for simultaneous detection of two oxidation states of iron in living cells and in brain slices of transgenic AD mice.

Recently, it has been demonstrated that ferroptosis increases the total labile iron pool that contains both Fe^{2+} and Fe^{3+} due to degradation of the Fe^{3+} -storage protein ferritin in lysosomes, causing labile iron overload (82, 83). We monitored the iron distribution during ferroptosis and observed a similar increase of total iron. Our sensors provided the first piece of information for iron redox changes during ferroptosis (Fig. 3). An increase in the overall labile iron pool was observed within 4 hours when inducing ferroptosis with RSL3. After 4 hours of ferroptosis, a decrease of both Fe^{2+} and Fe^{3+} was observed, which suggests a depletion of labile iron from the endosomal-lysosomal system in the later stage of ferroptosis. This reduction could be induced by STEAP3 or other endogenous metalloreductases, while the initial increase of Fe^{3+} is possibly from the release of ferritin-bound Fe^{3+} (65). In addition, a decrease in the $\text{Fe}^{3+}/\text{Fe}^{2+}$ ratio was observed over time, and such an observation reveals a potential role of iron redox cycling, which may serve as a source of oxidative stress, during ferroptosis. This conclusion is consistent with oxidative stress accumulation during ferroptosis, an iron-dependent cell death pathway (84).

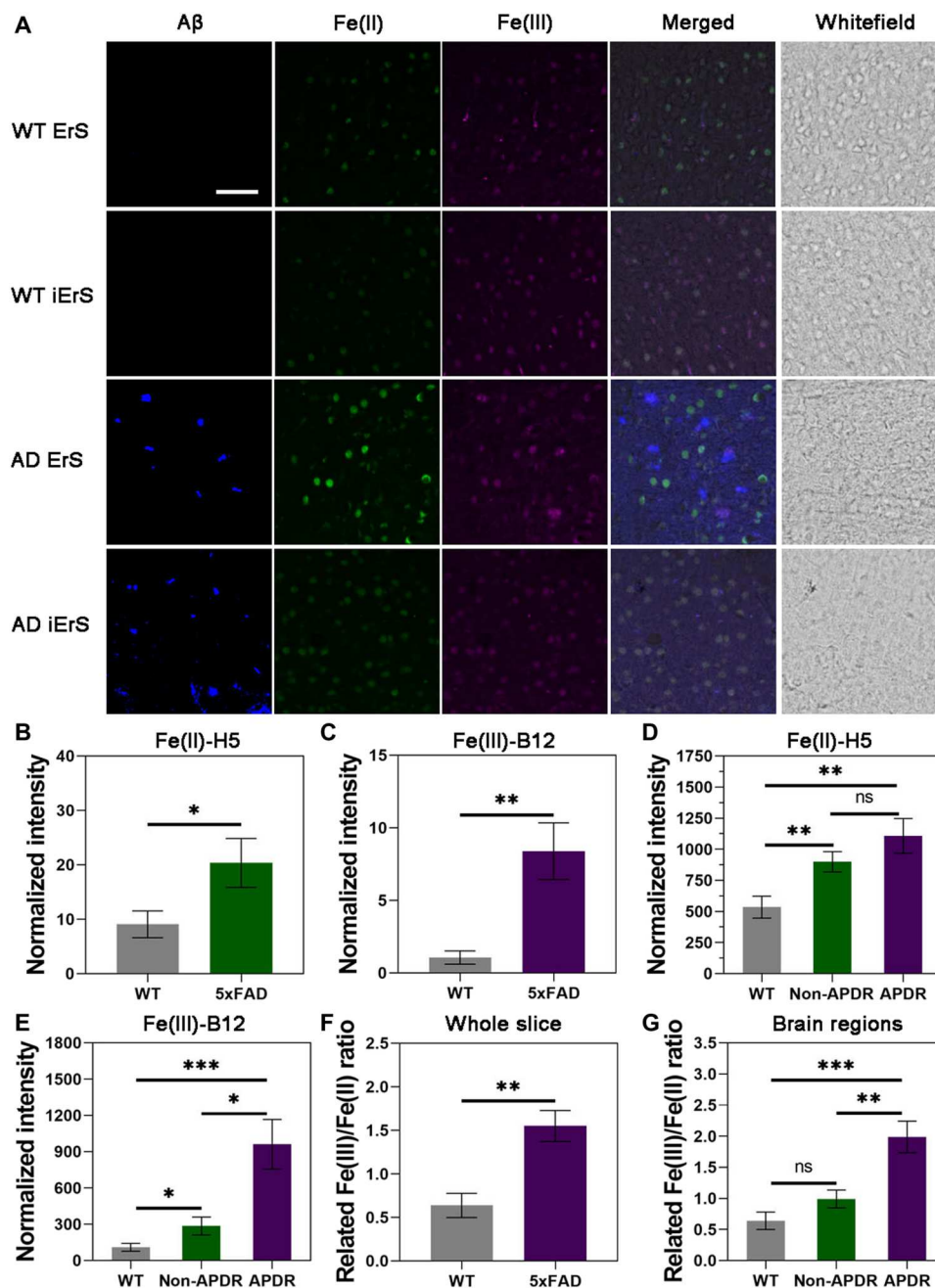


Fig. 4. $\text{Fe}^{3+}/\text{Fe}^{2+}$ ratio increases in brain regions containing amyloid plaques. (A) Both Fe^{2+} and Fe^{3+} were monitored in 11-month-old mouse brain slices that immunostained with the HJ3.4 antibody, which labels immunoreactive $\text{A}\beta$ plaques, to trace the colocalization between iron and $\text{A}\beta$ plaques in mouse brains. ErS, the active version of iron sensors containing the enzyme (E) strand and the substrate strand with the ribonucleotide as the cleavage site (rS); iErS, the inactive DNAzyme sensor control, which contains a point mutation in the enzyme strand that renders the DNAzyme inactive in the presence of Fe^{2+} or Fe^{3+} . The signal from iErS is considered as background signal that is caused by auto fluorescence or Fe^{2+} - or Fe^{3+} -independent cleavages (B and C) Statistical analysis of fluorescence intensity in (A). Fluorescent signals were normalized by subtracting the background detected with inactive DNAzyme sensors. Both Fe^{2+} (B) and Fe^{3+} (C) levels were elevated in 5xFAD mice when compared with wild-type (WT) controls. (D) When monitoring the distribution of Fe^{2+} and Fe^{3+} and comparing with WT mouse brains, Fe^{2+} level was elevated 2.1-fold in the cortex regions with $\text{A}\beta$ plaques (APDR) and was elevated 1.7-fold in the surrounding cortex regions that did not show $\text{A}\beta$ plaque deposition signal (non-APDR). (E) Fe^{3+} increased more (8.7-fold) in APDR than the non-APDR (2.6-fold). (F) The $\text{Fe}^{3+}/\text{Fe}^{2+}$ ratio showed increase in whole-brain slices of WT and 5xFAD mice. (G) Most of the increased $\text{Fe}^{3+}/\text{Fe}^{2+}$ ratio was in the APDR but not non-APDR in 5xFAD mouse cortex. Scale bar, 50 μm . Analyzed with paired Student's *t* test. * $P < 0.05$, ** $P < 0.01$, and *** $P < 0.001$. ns, not significant.

As a key player in redox biology, iron is also involved in the generation of reactive oxygen species from A β (79). By using our DNAzyme-based sensors, we observed elevated iron signals that colocalized with aggregated A β plaques (Fig. 4, A, D, and E). The observations on both total iron increase and the distribution patterns are consistent with earlier reports demonstrating increase in the level of iron in AD brain slices stained with potassium ferricyanide/ferrocyanide or as detected by magnetic resonance imaging (MRI) (18, 22, 85). Although these previous works reported similar increases in cerebral iron accumulation around A β , here, we are able to visualize both Fe²⁺ and Fe³⁺ simultaneously in single brain slices, allowing observation of the spatial relationship between the two oxidation states. In addition, our iron-specific DNAzyme-based sensors allow us to obtain spatial information about iron redox ratios, revealing a significant increase in the Fe³⁺/Fe²⁺ ratio surrounding amyloid plaque regions but not in other brain regions (Fig. 4G). Our data suggest that not only total iron but also iron redox cycling is involved in the progression of AD. Combining these data with our observation that both Fe²⁺ and Fe³⁺ levels increased around A β plaque regions and suggests a potential role of A β plaques in accumulating Fe³⁺ over Fe²⁺ from surrounding cells and/or proteins in AD mouse brains. The elevated levels of iron surrounding A β plaques might be derived from labile iron pools that contribute to the formation of iron-A β adducts or transchelation of iron from ferritin by A β plaques during AD progression due to the potential interaction between iron and A β plaques, instead of simply changing the oxidation states between different forms of iron (86, 87). However, it is unknown whether the dysregulated iron is involved in amyloid plaque formation, or this is a secondary effect of amyloid plaque formation in this mouse model. Overall, our data demonstrate that our DNAzyme-based iron sensors can provide unique and powerful tools for studying the intracellular dynamics of iron redox states and have the potential to open new avenues to further investigate different biological processes that involve redox metal ions and understand their roles in several neurodegenerative diseases such as AD.

MATERIALS AND METHODS

Materials

DNA sequences

All DNA was ordered from Integrated DNA Technologies (IDT). Modifications are indicated with IDT's modification codes (see table S4).

Buffers

Fe²⁺ buffer contains 50 mM bis-tris and 400 mM NaCl at pH 7.0 (adjusted with HCl). Fe³⁺ buffer contains 40 mM sodium acetate, 5 mM bis-tris, and 200 mM NaCl at pH 5.5 (adjusted with HNO₃). Universal Fe buffer contains 20 mM sodium acetate, 5 mM bis-tris, and 200 mM NaCl at pH 6.0.

In vitro selection of Fe²⁺-dependent DNAzymes

The initial pool used for all four different selection conditions was identical, using a randomized N50 region flanked by two primer-binding regions, of which one contained the single riboadenosine to serve as a cleavage site. A P2-iSp primer contained a hexaethylene glycol spacer (Spacer-C18, from IDT) modification, which stops Taq polymerization reaction from further extension, was used during the polymerase chain reaction (PCR) amplification step.

The internal C18 spacer is followed by AACACAACAACAAC, which results in production of the antisense strand with 15 nucleotides longer than the sense strand (DNA random pool). Therefore, single-stranded DNA random pools were separated from the antisense strand using denaturing polyacrylamide gel electrophoresis (PAGE).

The initial random pool for the first selection round was generated in two steps using a PCR thermocycler (C1000 Touch Thermal Cycler from Bio-Rad Laboratories Inc.). PCR1 was carried out in 96 PCR tubes with 0.1 μ M IDT DNA template in three steps. In the first step, 0.1 μ M primer P2-iSp was added to the PCR mixture containing 0.1 μ M DNA template to undergo two cycles of extension. The second step was carried out by the addition of 0.15 μ M primer P1 and two more extension cycles. Last, in the third step, 0.9 μ M primer P2-iSp was added, and 10 cycles of extension were carried out. PCR2 was conducted by the addition of 1 μ M primer P3 (for incorporation of the RNA base) and 0.1 μ M primer P2-iSp, followed by 10 cycles of amplification. Before the PCR2 reaction was performed, 2 μ l of [α -³²P]-dATP (PerkinElmer) was added to label the DNA strands. The PCR products were then precipitated with 10% of a 3 M sodium acetate solution, at pH 5.2, and 2.7 \times volume of cold ethanol. The samples were stored at -80°C for at least 1 hour and then centrifuged, washed, and lyophilized. Note that subsequent PCR amplifications, which were used to amplify selected DNA at the end of each selection round, were slightly different. In those reactions, PCR1 was carried out in a single step with 1 μ M P2-iSp and P2 primers, followed by PCR2 using 5% of the PCR1 reaction as DNA template with 0.1 μ M primer P2-iSp and 1 μ M P3.

Ethanol-precipitated PCR products were dissolved in water, and an equal amount of stop buffer was added before loading samples on the gel. The stop buffer contained 8 M urea, 50 mM EDTA, and 1 \times TBE (tris, boric acid, and EDTA). The reaction products were purified using a 10% denaturing PAGE gel, with the use of 1 \times TBE as the running buffer. The PCR product was run on the PAGE gel alongside DNA size markers corresponding to the cleaved (87-mer) and intact (110-mer) pool. The gel was then covered with a plastic wrap; a radioactive triangle location marker was placed on top, and the gel was exposed to a phosphorimager cassette. After imaging the exposed film, bands that corresponded to the 110-mer marker on the gel was excised, crushed, and extracted with a solution containing 10 mM tris, 0.1 mM EDTA, and 300 mM sodium chloride (extraction buffer). Gel particles were frozen over 10 min at -80°C and thawed in a room temperature water bath for at least 5 min to improve the extraction process. The solution was centrifuged at 10,000g for 1 min to obtain a gel-free DNA in the extraction buffer. DNA samples were ethanol-precipitated using the aforementioned procedure.

The dried pools acquired from initial pool generation for the first selection round (and for PCR amplifications of subsequent selection rounds) were redissolved in 1 \times selection buffer and incubated with a desired concentration of Fe²⁺ for positive selections or a mixture of competing divalent metal ions (for counter selections) for 18 hours. Fe²⁺ concentration and incubation time at each round of the selection are indicated in tables S5 and S6. An initial negative selection was carried out before round 1 by incubating the DNA pool in selection buffer in the absence of divalent metal ions for 24 hours. Counter selections were carried out by incubating the DNA pools with 1 mM Mn²⁺, Cd²⁺, Zn²⁺, and Co²⁺ and 0.2 mM Pb²⁺ in selection buffer over 18 hours. Overall, four different

selection conditions were carried out and each condition named with a letter (E to H; see table S1). After negative and counter selection steps, uncleaved DNA pools were PAGE-purified and used for the subsequent positive selection. Cleaved DNA produced in each positive selection was PAGE-purified and used as a PCR template for a subsequent round of the selection. The stringency of positive selections was gradually increased by decreasing the reaction time and decreasing Fe^{2+} concentration as the selection progressed (tables S5 and S6). All selection reactions were quenched by the addition of the stop buffer (50% final volume). All PAGE purifications were carried out using a 10% denaturing gel alongside the DNA size markers used earlier.

In vitro selection of Fe^{3+} -dependent DNAzymes

Similar to the selection of Fe^{2+} -DNAzymes, in vitro selection for Fe^{3+} -dependent DNAzymes was carried out using a denaturing PAGE-based purification method to separate cleavage products from uncleaved pools based on their size difference. In vitro selection was performed at pH 5.5 using rG as the cleavage site. Moreover, two different DNA pools with random region size of 35 or 50 nucleotides were used. The initial selection pools were generated through single linear PCR amplification. The PCR templates, synthesized by IDT, were designed with the goal of eliminating the need for multiple PCR amplifications to generate the initial sequence pools. DNA pools were generated by linear amplification of 360 pmol of the template mixed with 3.6 nmol of P3 primer in 90 PCR tubes (40 μl each), followed by 10 thermal cycles to complete the pool generation (40 s at 94°C, 1.25 min at 53°C, and then 1.1 min at 72°C). In the generation of each pool, 4 μl of [α - ^{32}P]-dATP was used to internally label PCR products with ^{32}P . Amplification of the selected pools after each positive selection round was carried out through two PCR reactions. In addition to the template and primers, each PCR reaction included Taq DNA polymerase (0.1 U/ μl ; NEB), 1.5 mM MgCl_2 , 50 mM KCl, 10 mM tris-HCl (pH 8.3 at 25°C), and each deoxynucleoside triphosphate (dNTP) at 0.2 mM. Note that all parameters of different PCR reactions were optimized before the initiation of the in vitro selection. This optimization process was required to minimize production of side products, obtain clean products, and increase yield of the correct PCR product. DNA pools were PAGE-purified using the same protocol described in the "In vitro selection of Fe^{2+} -dependent DNAzymes" section.

Dried pools were dissolved in 1 \times selection buffer and incubated for 24 hours (negative selection). This step was carried out before all positive selection steps unless stated. Negative selection steps were carried out to remove nonspecific cleavage that may occur in an Fe^{3+} -independent manner. After the negative selection, uncleaved pools were PAGE-purified, extracted from gel, ethanol-precipitated, and dried to be used for positive selection. Dried pools were dissolved in 1 \times selection buffer and mixed with desired concentration of Fe^{3+} (for positive selections) for a certain period of time (table S7). To initiate selection, Fe^{3+} was dissolved in selection buffer to make 2 \times Fe^{3+} stock solution. Then, equal volume of DNA samples were mixed with the 2 \times Fe^{3+} stock solution. The 2 \times Fe^{3+} solutions were prepared right before the positive selection. All positive selections were carried out in the dark by covering tubes with aluminum foil to prevent unwanted light-induced DNA cleavage by Fe^{3+} . After round 4, each of the in vitro selection experiments carried out with the rG cleavage site at pH 5.5 were branched into

two conditions by continuing or not continuing negative selection steps (see table S7). Cleaved DNA obtained in each positive selection was PAGE-purified and used as template for PCR amplification reactions to generate DNA pools for the next round of the selection. Stringency of positive selections was gradually increased by decreasing both the reaction time and Fe^{3+} concentration (table S7). All selection reactions were quenched with an equal volume of stop buffer. All PAGE purifications were carried out using a 10% gel alongside the DNA size markers used earlier.

Cloning and sequencing

On the basis of (i) the cleavage activity of the selected pools, (ii) results obtained in control experiments, and (iii) the activity assays carried out with different Fe^{2+} or Fe^{3+} concentrations, the most active pools with lowest background activity were chosen for cloning and sequencing. Cloning was carried out using PCR products with primers with no ribonucleotide cleavage site or Taq stopper. The same PCR reactions were carried out using selection primers to control activity of the species used for cloning. Negative PCR controls, with no template, were performed to assure that the observed amplifications were not caused by a contamination.

DNA sequences obtained from sequencing aligned on the basis of their sequence similarity for each individual pool. Sequence identity of the thermodynamically stable DNA tetraloop, which was engineered in the design of the random pools, remained intact in more than 96% of the obtained clones for the Fe^{3+} -dependent selection. Among 149 individual sequences obtained from Fe^{2+} -dependent selections, only 38 of them contain the intact tetraloop, with the rest of the clones having at least one mutation in this region. Few sequences were identified with mutations in their primer regions. Conservation of the stable tetraloop suggests that formation of this stable structure did not interfere with catalytic activity of the evolved sequences, while relatively high variation in the tetraloop region might imply that formation of this stable structure was not in favor of forming catalytically active structures. Because this region in the Fe^{2+} pool was not part of the PCR primers and considering the error rate of Taq DNA polymerase, a potential selection pressure might have caused evolution of species without the stable tetraloop over several selection rounds. The presence of the tetraloop in the active sequences can help in the prediction of active secondary structures. The sequence similarity of obtained sequences was represented using sequence similarity networks, originally used for organizing sequence similarity of protein sequences.

In vitro activity assays of Fe(II)-H5 and Fe(III)-B12 DNAzymes

In vitro activity assays were performed by incubating a solution of the DNAzymes with the indicated amount of metal solution (typically in a 1:1 volume ratio) and measuring the fluorescence change over time with a fluorometer. Metal stocks were prepared from ferric nitrate [$\text{Fe}(\text{NO}_3)_3$] and ferrous chloride (FeCl_2) dissolved in HNO_3 or HCl , respectively, which were then diluted into the relevant buffer. Both the metal solutions and the DNAzyme solutions were prepared in the relevant buffers so that there was no effect from different buffers mixing during the reaction, and their pH was checked to make sure that the solutions remained at the desired pH (especially important for the higher metal concentrations). For aerobic conditions, a SpectraMax M2 multidetection reader was used from the Roy J. Carver Biotechnology Center at the

Metabolomics Center. For anaerobic conditions, a DeNovix QFX portable fluorometer was used inside of an anaerobic glove box. In addition, the metal selectivity tests were all performed with the DeNovix QFX fluorometer for consistency. For the SpectraMax M2, excitation at 633 nm and emission at 665 to 750 nm were used. For the DeNovix QFX, excitation at 470 nm and emission at 514 to 567 nm were used for the Fe(II)-H5 DNAzyme, and excitation at 635 nm and emission at 665 to 740 nm were used for the Fe(III)-B12 DNAzyme. Before the assay, the enzyme and substrate strands were annealed together using a water bath $>65^{\circ}\text{C}$ for 5 min and then cooled to room temperature for 30 min. The fluorescence intensity in the presence of different metal ions was normalized to the fluorescent signal without addition of divalent or trivalent metal ions (i.e., just buffer) at the 30-min time point, for a direct comparison.

Cell culture, sensor delivery, and colocalization study

Iron-deficient buffer was prepared by S. McMasters of the University of Illinois School of Chemical Sciences Cell Media Facility as a standard preparation of minimum essential medium (MEM) but without fetal bovine serum (FBS) or any added iron (from Tf) to remove any potential contaminating iron species. HepG2 cells were purchased from the American Type Culture Collection (HB-8065), and was cultured in Dulbecco's modified Eagle's medium (DMEM) with adding 10% FBS, penicillin (100 U/ml), and streptomycin (100 U/ml), and in a 5% CO_2 , 37°C incubator. A hemocytometer was used to determine cell density.

For delivery of DNAzyme sensors using PEI (66, 67), the corresponding Fe(II)-H5-ErS, Fe(II)-H5-iErS, Fe(III)-B12-ErS, and Fe(III)-B12-iErS (final concentration of 10 μM) were mixed in the Fe^{2+} buffer and Fe^{3+} buffer separately. The mixtures were annealed at 95°C for 5 min and stored at room temperature to allow full hybridization. PEI (25 kDa) was dissolved in water at 1 mg/ml. For the active enzyme group, 2 μl of PEI was mixed and incubated with 2 μl of 10 μM Fe(II)-H5-ErS and Fe(III)-B12-ErS for 30 min in iron-deficient medium to allow the formation of PEI-DNA complexes (PEI-ErS) with the optimal N/P ratio (moles of amine, N, from the cationic polymer to moles of phosphate, P, from the DNA) as suggested previously (66). For the inactive enzyme group, 2 μl of PEI was mixed and incubated with 2 μl of 10 μM Fe(II)-H5-iErS and Fe(III)-B12-iErS in iron-deficient medium for 30 min to allow the formation of PEI-DNA complexes (PEI-iErS). The normal cell medium was replaced with iron-deficient medium before the PEI-ErS or PEI-iErS was added to the cells grown in the plates.

After incubating HepG2 cells with PEI-ErS or PEI-iErS complex for 4 hours, cells were washed with phosphate-buffered saline (PBS) twice to remove excess amounts of complexes in medium. Then, the cells were stained by Hoechst 33258 for 15 min. Images were obtained using a Zeiss LSM 880 confocal microscope at $63\times$ oil objective lens with numerical aperture 1.40 and immersion medium Immersol 518 F (Zeiss) at the UIUC IGB Core Facilities. Fluorescence emission of Hoechst 33258 was measured over 450 to 500 nm with excitation at 401 nm. Fe(II)-H5 was excited by 488 nm and measured over 500 to 550 nm, and Fe(III)-B12 was excited at 633 nm and measured over 640 to 700 nm. A laser power of 67% and pinhole size of 1 atomic unit (AU) were used for the cellular images. Acquired images were analyzed by ImageJ using JACoP (88, 89). No background subtraction, Z-stacks, Gaussian blur filter, or change

thresholds were performed for visualizing the figures. For cell fluorescence quantification, we quantified the average fluorescence signals intensity in five cells (for TurboFect transfected cells) or five LysoTracker-labeled regions in different cells (for PEI transfected cells), per picture and three pictures per group with Image J (88), for the statistical comparison between groups.

FerroOrange was used at the final concentration of 1 μM , following the standard protocol from Sigma-Aldrich. When delivering FerroOrange with PEI, the same final concentration of FerroOrange was mixed with 2 μl of PEI and incubated at room temperature for 30 min before transfecting the cells. When delivering the DNAzymes with TurboFect, 100 pmol of DNAzyme S strand was annealed with 110 pmol of E strand in cells with 5 mM bis-tris, 40 mM sodium acetate, and 200 mM sodium chloride (pH 5.5) and then diluted with 98 μl of Opti-MEM and 1 μl of TurboFect transfection reagent. The mixture was incubated at room temperature for 20 min and incubated with cells for 4 hours. Afterward, the cells were washed with $1\times$ Hanks' balanced salt solution (HBSS) and stained with Hoechst 33342 before imaging.

Simultaneous imaging of labile Fe^{2+} and Fe^{3+} in living cells

HepG2 or HeLa cells were cultured in glass-bottom dishes until about 70% confluence. The cells were pretreated with iron-deficient MEM containing either 100 μM DFO, 100 μM ferric ammonium citrate, 5 μM holo-Tf, or 50 μM Tf for 4 hours, and then, the medium was replaced with an iron-deficient MEM containing PEI-ErS or PEI-iErS complexes or Opti-MEM containing 1 μl of TurboFect transfection reagent as described in the "Cell culture, sensor delivery, and colocalization study" section for 4 hours. Before imaging, the cells were stained by LysoTracker Red and Hoechst 33258 for 15 min. After washing with PBS, the cells were incubated in iron-deficient MEM or regular DMEM, respectively, during the imaging.

Ferroptosis-induced fluctuations of labile Fe^{2+} and Fe^{3+} pools

HepG2 cells were treated with 1 μM RSL3 in normal MEM at different time points (0, 2, 4, 6, 8, and 10 hours). Then, the cell medium was replaced by iron-deficient MEM containing PEI-ErS or PEI-iErS and incubated in a 37°C , 5% CO_2 incubator for another 4 hours. Before imaging, the cells were stained by LysoTracker Red and Hoechst 33258 for 15 min. After washing with PBS, the cells were incubated in iron-deficient MEM during the imaging.

To measure the cytotoxicity of RSL3 to HepG2 cells, a standard MTT assay was used. HepG2 cells were seeded at a density of 15,000 cells per well in 96-well plates. When the cells grew to 80% confluence, the medium was replaced by the normal MEM containing 1 μM RSL3 at different time points (0, 2, 4, 6, 8, and 10 hours). Afterward, the cell medium was replaced by the iron-deficient MEM containing PEI-ErS or PEI-iErS, incubated in a 37°C , 5% CO_2 incubator for another 4 hours. The absorbance at 570 nm was measured with a SpectraMax M2 microplate reader to obtain the MTT assay readings. The untreated cells were set as a blank control for normalization.

Fe^{2+} and Fe^{3+} detection in mouse brain slices

All animal studies were performed with the approval of the Institutional Animal Care and Use Committee (IACUC) of the University of Illinois at Urbana-Champaign (protocol number 22094) and the

IACUC of the University of Texas at Austin (protocol number AUP-2021-00295). Eleven-month-old 5xFAD mice (RRID: MMRRRC_034840-JAX) and WT mice (B6SJLF1/J) of the same sex were used and compared. To obtain the brain slices, after deep anesthesia, the mice were perfused with saline, followed by paraformaldehyde fixation. The mouse brain was isolated and fixed in 4% paraformaldehyde for 24 hours at 4°C and then embedded in 30% sucrose in PBS for another 3 days. Coronal brain sections (section thickness, 50 μm) were obtained by microtome section and stored in cryoprotectant at -20°C before staining. Ten brain slices from three individuals were stained with technical repeats for each group. The brain sections were rinsed with PBS three times for 5 min each and then blocked with 2% bovine serum albumin (BSA) in PBS for 10 min. To visualize A β (1-13), brain slices were incubated with CF350-conjugated HJ3.4 antibody (78), which was pre-labeled with the Mix-n-Stain Antibody Labeling Kit (Sigma-Aldrich), with 1:500 dilution in blocking solution for 1 hour and then washed with 2% BSA in PBS for 4 min, followed by another wash in PBS for 5 min to remove extra antibody and non-specific signaling. To image Fe $^{2+}$ and Fe $^{3+}$ simultaneously, 2 μM DNAzyme enzyme strand and 2.2 μM DNAzyme substrate strand for both iron oxidization states were annealed separately in 5 mM bis-tris (pH 5.5), 40 mM sodium acetate, and 200 mM NaCl buffer (bis-tris-acetate buffer) by incubation at 95°C for 5 min and then slowly decreased to room temperature. After annealing, the Fe(II)-H5 and Fe(III)-B12 sensors were mixed in a 1:1 ratio to generate the sensor mix. The mouse brain sections prestained with HJ3.4 antibody were rinsed with the bis-tris-acetate buffer twice for 5 min each and then incubated in the sensor mix for 30 min. After incubation, the brain slices were rinsed once in the bis-tris-acetate buffer and mounted with Fluoromount-G mounting medium (SouthernBiotech, Birmingham, AL, USA). Images were taken with a Nikon spinning disk confocal or Zeiss LSM 710 confocal microscope with a 20 \times objective with 405-, 488-, and 640-nm channels. Afterward, images were processed and quantified with ImageJ as follows: To enable a direct comparison between groups without interference from a potential difference in background signaling between treatments, as indicated by the point-mutated inactive sensor (iErS), we normalized the fluorescent intensity of our sensor with iErS groups by subtracting the average fluorescence intensity in the imaging area or the regions of interest (APDR or non-APDR regions) in the pictures of correlated iErS group from the ErS group with the same treatment. Colocalization study and quantification of fluorescence intensity for APDR and non-APDR regions were performed by marking the region of interests on the basis of HJ3.4 staining. Five spots including four corners and the center of each image were analyzed. Three images were taken for each group.

Data processing and statistical analysis

To have a direct comparison of the iron amount between groups, we normalized the background signals by subtracting the fluorescence signals in iErS groups from the ErS groups ($F - F_0$). No Z-stacks or change thresholds were used for statistical analysis. Graphs were plotted with GraphPad (GraphPad Software Inc.) or Origin (Origin-Labs Corporation) and correspond to a single experiment. Bars represent means \pm SEM. Two-tailed distribution and two-sample equal variance t test were used for analyzing significance. Dixon's Q tests were performed to identify and exclude outliers. $*P < 0.05$, $**P < 0.01$, and $***P < 0.001$. All experiments have three or more

biological replicates, which showed the same conclusion. The presented data described the quantification from single representative replicates from those biological replicates.

Supplementary Materials

This PDF file includes:

Figs. S1 to S33
Tables S1 to S7
References

[View/request a protocol for this paper from Bio-protocol.](#)

REFERENCES AND NOTES

- D. Galaris, A. Barbouti, K. Pantopoulos, Iron homeostasis and oxidative stress: An intimate relationship. *Biochim. Biophys. Acta Mol. Cell Res.* **1866**, 118535 (2019).
- N. Kim, H. J. Lee, Redox-active metal ions and amyloid-degrading enzymes in Alzheimer's disease. *Int. J. Mol. Sci.* **22**, 7697 (2021).
- E. L. Que, D. W. Domaille, C. J. Chang, Metals in neurobiology: Probing their chemistry and biology with molecular imaging. *Chem. Rev.* **108**, 1517–1549 (2008).
- K. P. Carter, A. M. Young, A. E. Palmer, Fluorescent sensors for measuring metal ions in living systems. *Chem. Rev.* **114**, 4564–4601 (2014).
- J. M. Braugher, L. A. Duncan, R. L. Chase, The involvement of iron in lipid peroxidation. Importance of ferric to ferrous ratios in initiation. *J. Biol. Chem.* **261**, 10282–10289 (1986).
- S. J. Dixon, K. M. Lemberg, M. R. Lamprecht, R. Skouta, E. M. Zaitsev, C. E. Gleason, D. N. Patel, A. J. Bauer, A. M. Cantley, W. S. Yang, B. Morrison, B. R. Stockwell, Ferroptosis: An iron-dependent form of nonapoptotic cell death. *Cell* **149**, 1060–1072 (2012).
- B. R. Stockwell, J. P. Friedmann Angeli, H. Bayir, A. I. Bush, M. Conrad, S. J. Dixon, S. Fulda, S. Gascón, S. K. Hatzios, V. E. Kagan, K. Noel, X. Jiang, A. Linkermann, M. E. Murphy, M. Overholtzer, A. Oyagi, G. C. Pagnussat, J. Park, Q. Ran, C. S. Rosenfeld, K. Salnikow, D. Tang, F. M. Torti, S. V. Torti, S. Toyokuni, K. A. Woerpel, D. D. Zhang, Ferroptosis: A regulated cell death nexus linking metabolism, redox biology, and disease. *Cell* **171**, 273–285 (2017).
- A. Ashraf, J. Jeandriens, H. G. Parkes, P.-W. So, Iron dyshomeostasis, lipid peroxidation and perturbed expression of cystine/glutamate antiporter in Alzheimer's disease: Evidence of ferroptosis. *Redox Biol.* **32**, 101494 (2020).
- N. Yan, J. Zhang, Iron metabolism, ferroptosis, and the links with Alzheimer's disease. *Front. Neurosci.* **13**, 1443 (2020).
- Z. Shen, J. Song, B. C. Yung, Z. Zhou, A. Wu, X. Chen, Emerging strategies of cancer therapy based on ferroptosis. *Adv. Mater.* **30**, e1704007 (2018).
- T. Xu, W. Ding, X. Ji, X. Ao, Y. Liu, W. Yu, J. Wang, Molecular mechanisms of ferroptosis and its role in cancer therapy. *J. Cell. Mol. Med.* **23**, 4900–4912 (2019).
- A. Spolaor, P. Vallelonga, J. Gabrieli, G. Cozzi, C. Boutron, C. Barbante, Determination of Fe $^{2+}$ and Fe $^{3+}$ species by FIA-CRC-ICP-MS in Antarctic ice samples. *J. Anal. At. Spectrom.* **27**, 310–317 (2012).
- Q. Hu, Simultaneous separation and quantification of iron and transition species using LC-ICP-MS. *Am. J. Anal. Chem.* **2**, 675–682 (2011).
- N. Mironova-Ulmane, M. Polakov, A. Pavlenko, T. Zvagule, M. Eglite, E. Churbakova, N. Kurjane, T. Kärner, "The Optical And Epr Spectra of Fe $^{2+}$ and Fe $^{3+}$ Ions in the Blood of the Chernobyl Clean-Up Worker" in *World Congress on Medical Physics and Biomedical Engineering 2006*, R. Magjarevic, J. H. Nagel, Eds. (Springer, 2007), *IFMBE Proceedings*, pp. 2096–2098.
- S. Sasaki, Fe $^{2+}$ and Fe $^{3+}$ ions distinguishable by x-ray anomalous scattering: Method and its application to magnetite. *Rev. Sci. Instrum.* **66**, 1573 (1995).
- R. J. Ogg, J. W. Langston, E. M. Haacke, R. G. Steen, J. S. Taylor, The correlation between phase shifts in gradient-echo MR images and regional brain iron concentration. *Magn. Reson. Imaging* **17**, 1141–1148 (1999).
- O. Dietrich, J. Levin, S.-A. Ahmadi, A. Plate, M. F. Reiser, K. Bötzel, A. Giese, B. Ertl-Wagner, MR imaging differentiation of Fe $^{2+}$ and Fe $^{3+}$ based on relaxation and magnetic susceptibility properties. *Neuroradiology* **59**, 403–409 (2017).
- L. H. P. Vroegindewij, L. Bossoni, A. J. W. Boon, J. H. P. Wilson, M. Bulk, J. Labra-Muñoz, M. Huber, A. Webb, L. van der Weerd, J. G. Langendonk, Quantification of different iron forms in the aceruloplasminemia brain to explore iron-related neurodegeneration. *NeuroImage Clin.* **30**, 102657 (2021).

19. W. Breuer, S. Epsztejn, Z. I. Cabantchik, Iron acquired from transferrin by K562 cells is delivered into a cytoplasmic pool of chelatable iron(II). *J. Biol. Chem.* **270**, 24209–24215 (1995).
20. O. Kakhlon, Z. I. Cabantchik, The labile iron pool: Characterization, measurement, and participation in cellular processes. This article is part of a series of reviews on "Iron and Cellular Redox Status." The full list of papers may be found on the homepage of the journal. *Free Radic. Biol. Med.* **33**, 1037–1046 (2002).
21. M. Kruszewski, Labile iron pool: The main determinant of cellular response to oxidative stress. *Mutat. Res.* **531**, 81–92 (2003).
22. M. A. Smith, P. L. R. Harris, L. M. Sayre, G. Perry, Iron accumulation in Alzheimer disease is a source of redox-generated free radicals. *Proc. Natl. Acad. Sci. U.S.A.* **94**, 9866–9868 (1997).
23. H. Y. Au-Yeung, J. Chan, T. Chantarojsiri, C. J. Chang, Molecular imaging of labile iron(II) pools in living cells with a turn-on fluorescent probe. *J. Am. Chem. Soc.* **135**, 15165–15173 (2013).
24. A. T. Aron, M. O. Loehr, J. Bogena, C. J. Chang, An endoperoxide reactivity-based FRET probe for ratiometric fluorescence imaging of labile iron pools in living cells. *J. Am. Chem. Soc.* **138**, 14338–14346 (2016).
25. T. Hirayama, H. Tsuboi, M. Niwa, A. Miki, S. Kadota, Y. Ikeshita, K. Okuda, H. Nagasawa, A universal fluorogenic switch for Fe(II) ion based on N-oxide chemistry permits the visualization of intracellular redox equilibrium shift towards labile iron in hypoxic tumor cells. *Chem. Sci.* **8**, 4858–4866 (2017).
26. T. Hirayama, M. Niwa, S. Hirotsawa, H. Nagasawa, High-throughput screening for the discovery of iron homeostasis modulators using an extremely sensitive fluorescent probe. *ACS Sens.* **5**, 2950–2958 (2020).
27. A. T. Aron, M. C. Heffern, Z. R. Lonergan, M. N. Vander Wal, B. R. Blank, B. Spangler, Y. Zhang, H. M. Park, A. Stahl, A. R. Renslo, E. P. Skaar, C. J. Chang, In vivo bioluminescence imaging of labile iron accumulation in a murine model of *Acinetobacter baumannii* infection. *Proc. Natl. Acad. Sci. U.S.A.* **114**, 12669–12674 (2017).
28. R. K. Muir, N. Zhao, J. Wei, Y.-H. Wang, A. Moroz, Y. Huang, Y.-C. Chen, R. Sriram, J. Kurhanewicz, D. Ruggiero, A. R. Renslo, M. J. Evans, Measuring dynamic changes in the labile iron pool in vivo with a reactivity-based probe for positron emission tomography. *ACS Cent. Sci.* **5**, 727–736 (2019).
29. T. Hirayama, A. Miki, H. Nagasawa, Organelle-specific analysis of labile Fe(II) during ferroptosis by using a cocktail of various colour organelle-targeted fluorescent probes. *Metallomics* **11**, 111–117 (2019).
30. R. R. Breaker, G. F. Joyce, A DNA enzyme that cleaves RNA. *Chem. Biol.* **1**, 223–229 (1994).
31. Y. Li, R. R. Breaker, Deoxyribozymes: New players in the ancient game of biocatalysis. *Curr. Opin. Struct. Biol.* **9**, 315–323 (1999).
32. J. Li, W. Zheng, A. H. Kwon, Y. Lu, In vitro selection and characterization of a highly efficient Zn(II)-dependent RNA-cleaving deoxyribozyme. *Nucleic Acids Res.* **28**, 481–488 (2000).
33. Y. Lu, New transition metal-dependent DNAzymes as efficient endonucleases and as selective metal biosensors. *Chemistry* **8**, 4588–4596 (2002).
34. M. Cepeda-Plaza, E. L. Null, Y. Lu, Metal ion as both a cofactor and a probe of metal-binding sites in a uranyl-specific DNAzyme: A uranyl photocleavage study. *Nucleic Acids Res.* **41**, 9361–9370 (2013).
35. K. Hwang, P. Hosseinzadeh, Y. Lu, Biochemical and biophysical understanding of metal ion selectivity of DNAzymes. *Inorganica Chim. Acta.* **452**, 12–24 (2016).
36. R. J. Lake, Z. Yang, J. Zhang, Y. Lu, DNAzymes as activity-based sensors for metal ions: Recent applications, demonstrated advantages, current challenges, and future directions. *Acc. Chem. Res.* **52**, 3275–3286 (2019).
37. H. E. Ihm, Y. Lu, "In Vitro Selection of Metal Ion-Selective DNAzymes" in *Ribozymes. Methods in Molecular Biology*, J. S. Hartig, Ed. (Humana Press, 2012), vol. 848, pp. 297–316.
38. J. Li, Y. Lu, A highly sensitive and selective catalytic DNA biosensor for lead ions. *J. Am. Chem. Soc.* **122**, 10466–10467 (2000).
39. J. Liu, Y. Lu, Improving fluorescent DNAzyme biosensors by combining inter- and intramolecular quenchers. *Anal. Chem.* **75**, 6666–6672 (2003).
40. J. Liu, A. K. Brown, X. Meng, D. M. Crokep, J. D. Istok, D. B. Watson, Y. Lu, A catalytic beacon sensor for uranium with parts-per-trillion sensitivity and millionfold selectivity. *Proc. Natl. Acad. Sci. U.S.A.* **104**, 2056–2061 (2007).
41. J. Liu, Y. Lu, A DNAzyme catalytic beacon sensor for paramagnetic Cu²⁺ ions in aqueous solution with high sensitivity and selectivity. *J. Am. Chem. Soc.* **129**, 9838–9839 (2007).
42. J. Liu, Y. Lu, Rational design of "turn-on" allosteric DNAzyme catalytic beacons for aqueous mercury ions with ultrahigh sensitivity and selectivity. *Angew. Chem. Int. Ed. Engl.* **46**, 7587–7590 (2007).
43. T. Lan, K. Furuya, Y. Lu, A highly selective lead sensor based on a classic lead DNAzyme. *Chem. Commun. (Camb)* **46**, 3896–3898 (2010).
44. C. E. McGhee, K. Y. Loh, Y. Lu, DNAzyme sensors for detection of metal ions in the environment and imaging them in living cells. *Curr. Opin. Biotechnol.* **45**, 191–201 (2017).
45. Z. Yang, K. Y. Loh, Y.-T. Chu, R. Feng, N. S. R. Satyavolu, M. Xiong, S. M. Nakamata Huynh, K. Hwang, L. Li, H. Xing, X. Zhang, Y. R. Chemla, M. Gruebele, Y. Lu, Optical control of metal ion probes in cells and zebrafish using highly selective DNAzymes conjugated to upconversion nanoparticles. *J. Am. Chem. Soc.* **140**, 17656–17665 (2018).
46. Y. Lin, Z. Yang, R. J. Lake, C. Zheng, Y. Lu, Enzyme-mediated endogenous and bioorthogonal control of a DNAzyme fluorescent sensor for imaging metal ions in living cells. *Angew. Chem. Int. Ed. Engl.* **58**, 17061–17067 (2019).
47. E. M. McConnell, I. Cozma, Q. Mou, J. D. Brennan, Y. Lu, Y. Li, Biosensing with DNAzymes. *Chem. Soc. Rev.* **50**, 8954–8994 (2021).
48. S. Xing, Y. Lin, L. Cai, P. N. Basa, A. K. Shigemoto, C. Zheng, F. Zhang, S. C. Burdette, Y. Lu, Detection and quantification of tightly bound Zn²⁺ in blood serum using a photocaged chelator and a DNAzyme fluorescent sensor. *Anal. Chem.* **93**, 5856–5861 (2021).
49. W. Zhou, M. Vazin, T. Yu, J. Ding, J. Liu, In vitro selection of chromium-dependent DNAzymes for sensing chromium(III) and chromium(VI). *Chemistry* **22**, 9835–9840 (2016).
50. W. Zhou, R. Saran, P.-J. J. Huang, J. Ding, J. Liu, An exceptionally selective DNA cooperatively binding two Ca²⁺ ions. *ChemBiochem.* **18**, 518–522 (2017).
51. P.-J. J. Huang, J. Liu, Rational evolution of Cd²⁺-specific DNAzymes with phosphorothioate modified cleavage junction and Cd²⁺ sensing. *Nucleic Acids Res.* **43**, 6125–6133 (2015).
52. P. Bruesehoff, J. Li, A. J. Augustine 3rd, Y. Lu, Improving metal ion specificity during in vitro selection of catalytic DNA. *Comb. Chem. High Throughput Screen.* **5**, 327–335 (2002).
53. N. Carmi, L. A. Shultz, R. R. Breaker, In vitro selection of self-cleaving DNAs. *Chem. Biol.* **3**, 1039–1046 (1996).
54. S. W. Santoro, G. F. Joyce, A general purpose RNA-cleaving DNA enzyme. *Proc. Natl. Acad. Sci. U.S.A.* **94**, 4262–4266 (1997).
55. S. W. Santoro, G. F. Joyce, K. Sakthivel, S. Gramatikova, C. F. Barbas 3rd, RNA cleavage by a DNA enzyme with extended chemical functionality. *J. Am. Chem. Soc.* **122**, 2433–2439 (2000).
56. K. E. Nelson, P. J. Bruesehoff, Y. Lu, In vitro selection of high temperature Zn²⁺-dependent DNAzymes. *J. Mol. Evol.* **61**, 216–225 (2005).
57. R. Saran, J. Liu, A silver DNAzyme. *Anal. Chem.* **88**, 4014–4020 (2016).
58. C. E. McGhee, Z. Yang, W. Guo, Y. Wu, M. Lyu, C. J. DeLong, S. Hong, Y. Ma, M. G. McInnis, K. S. O'Shea, Y. Lu, DNAzyme-based lithium-selective imaging reveals higher lithium accumulation in bipolar disorder patient-derived neurons. *ACS Cent. Sci.* **7**, 1809–1820 (2021).
59. S.-F. Torabi, P. Wu, C. E. McGhee, L. Chen, K. Hwang, N. Zheng, J. Cheng, Y. Lu, In vitro selection of a sodium-specific DNAzyme and its application in intracellular sensing. *Proc. Natl. Acad. Sci. U.S.A.* **112**, 5903–5908 (2015).
60. S.-F. Torabi, Y. Lu, Identification of the same Na⁺-specific DNAzyme motif from two in vitro selections under different conditions. *J. Mol. Evol.* **81**, 225–234 (2015).
61. D. J. R. Lane, A. M. Merlot, M. L.-H. Huang, D.-H. Bae, P. J. Jansson, S. Sahni, D. S. Kalinowski, D. R. Richardson, Cellular iron uptake, trafficking and metabolism: Key molecules and mechanisms and their roles in disease. *Biochim. Biophys. Acta* **1853**, 1130–1144 (2015).
62. D. Richardson, P. Ponka, E. Baker, The effect of the iron(III) chelator, desferrioxamine, on iron and transferrin uptake by the human malignant melanoma cell. *Cancer Res.* **54**, 685–689 (1994).
63. R. C. Hider, X. Kong, Iron speciation in the cytosol: An overview. *Dalton Trans.* **42**, 3220–3229 (2013).
64. R. S. Ohgami, D. R. Campagna, A. McDonald, M. D. Fleming, The Steap proteins are metallo-reductases. *Blood* **108**, 1388–1394 (2006).
65. K. Pantopoulos, S. K. Porwal, A. Tartakoff, L. Devireddy, Mechanisms of mammalian iron homeostasis. *Biochemistry* **51**, 5705–5724 (2012).
66. Q.-Q. Zhao, J.-L. Chen, T.-F. Lv, C.-X. He, G.-P. Tang, W.-Q. Liang, Y. Tabata, J.-Q. Gao, N/P ratio significantly influences the transfection efficiency and cytotoxicity of a polyethylenimine/chitosan/DNA complex. *Biol. Pharm. Bull.* **32**, 706–710 (2009).
67. P. A. Longo, J. M. Kavran, M.-S. Kim, D. J. Leahy, Transient mammalian cell transfection with polyethylenimine (PEI). *Methods Enzymol.* **529**, 227–240 (2013).
68. R. V. Benjaminsen, M. A. Matthebjerg, J. R. Henriksen, S. M. Moghimi, T. L. Andresen, The possible "proton sponge" effect of polyethylenimine (PEI) does not include change in lysosomal pH. *Mol. Ther.* **21**, 149–157 (2013).
69. B. Chazotte, Labeling lysosomes in live cells with LysoTracker. *Cold Spring Harb. Protoc.* **2011**, pdb.prot5571 (2011).
70. FerroOrange Labile ferrous ion detecting probe | Goryo Chemical Inc. *FerroOrange Labile Ferr. Ion Detect. Probe Goryo Chem. Inc.*; <https://goryochemical.com/en/research-reagent/4703/>.
71. H. Feng, B. R. Stockwell, Unsolved mysteries: How does lipid peroxidation cause ferroptosis? *PLOS Biol.* **16**, e2006203 (2018).
72. W. S. Yang, B. R. Stockwell, Synthetic lethal screening identifies compounds activating iron-dependent, nonapoptotic cell death in oncogenic-RAS-harboring cancer cells. *Chem. Biol.* **15**, 234–245 (2008).

73. R. Shintoku, Y. Takigawa, K. Yamada, C. Kubota, Y. Yoshimoto, T. Takeuchi, I. Koshiishi, S. Torii, Lipoxigenase-mediated generation of lipid peroxides enhances ferroptosis induced by erastin and RSL3. *Cancer Sci.* **108**, 2187–2194 (2017).
74. X. Sui, R. Zhang, S. Liu, T. Duan, L. Zhai, M. Zhang, X. Han, Y. Xiang, X. Huang, H. Lin, T. Xie, RSL3 drives ferroptosis through GPX4 inactivation and ROS production in colorectal cancer. *Front. Pharmacol.* **9**, 1371 (2018).
75. T. Mosmann, Rapid colorimetric assay for cellular growth and survival: Application to proliferation and cytotoxicity assays. *J. Immunol. Methods* **65**, 55–63 (1983).
76. J.-L. Liu, Y.-G. Fan, Z.-S. Yang, Z.-Y. Wang, C. Guo, Iron and Alzheimer's disease: From pathogenesis to therapeutic implications. *Front. Neurosci.* **12**, 632 (2018).
77. H. Oakley, S. L. Cole, S. Logan, E. Maus, P. Shao, J. Craft, A. Guillozet-Bongaarts, M. Ohno, J. Disterhoft, L. Van Eldik, R. Berry, R. Vassar, Intraneuronal β -amyloid aggregates, neurodegeneration, and neuron loss in transgenic mice with five familial Alzheimer's disease mutations: potential factors in amyloid plaque formation. *J. Neurosci.* **26**, 10129–10140 (2006).
78. J. H. Roh, Y. Huang, A. W. Bero, T. Kasten, F. R. Stewart, R. J. Bateman, D. M. Holtzman, Sleep-wake cycle and diurnal fluctuation of amyloid- β as biomarkers of brain amyloid pathology. *Sci. Transl. Med.* **4**, 150ra122 (2012).
79. D. G. Smith, R. Cappai, K. J. Barnham, The redox chemistry of the Alzheimer's disease amyloid β peptide. *Biochim. Biophys. Acta* **1768**, 1976–1990 (2007).
80. J. Everett, E. Céspedes, L. R. Shelford, C. Exley, J. F. Collingwood, J. Dobson, G. van der Laan, C. A. Jenkins, E. Arenholz, N. D. Telling, Evidence of redox-active iron formation following aggregation of ferrihydrite and the Alzheimer's disease peptide β -amyloid. *Inorg. Chem.* **53**, 2803–2809 (2014).
81. J. Everett, E. Céspedes, L. R. Shelford, C. Exley, J. F. Collingwood, J. Dobson, G. van der Laan, C. A. Jenkins, E. Arenholz, N. D. Telling, Ferrous iron formation following the co-aggregation of ferric iron and the Alzheimer's disease peptide β -amyloid (1–42). *J. R. Soc. Interface* **11**, 20140165 (2014).
82. M. Gao, P. Monian, Q. Pan, W. Zhang, J. Xiang, X. Jiang, Ferroptosis is an autophagic cell death process. *Cell Res.* **26**, 1021–1032 (2016).
83. G. O. Latunde-Dada, Ferroptosis: Role of lipid peroxidation, iron and ferritinophagy. *Biochim. Biophys. Acta Gen. Subj.* **1861**, 1893–1900 (2017).
84. F. Kuang, J. Liu, D. Tang, R. Kang, Oxidative damage and antioxidant defense in ferroptosis. *Front. Cell Dev. Biol.* **8**, 586578 (2020).
85. J. M. G. van Bergen, X. Li, J. Hua, S. J. Schreiner, S. C. Steininger, F. C. Quevenco, M. Wyss, A. F. Gietl, V. Treyer, S. E. Leh, F. Buck, R. M. Nitsch, K. P. Pruessmann, P. C. M. van Zijl, C. Hock, P. G. Unschuld, Colocalization of cerebral iron with amyloid β in mild cognitive impairment. *Sci. Rep.* **6**, 35514 (2016).
86. N. D. Telling, J. Everett, J. F. Collingwood, J. Dobson, G. van der Laan, J. J. Gallagher, J. Wang, A. P. Hitchcock, Iron biochemistry is correlated with amyloid plaque morphology in an established mouse model of Alzheimer's disease. *Cell Chem. Biol.* **24**, 1205–1215.e3 (2017).
87. J. Everett, J. Brooks, F. Lermyte, P. B. O'Connor, P. J. Sadler, J. Dobson, J. F. Collingwood, N. D. Telling, Iron stored in ferritin is chemically reduced in the presence of aggregating A β (1–42). *Sci. Rep.* **10**, 10332 (2020).
88. C. A. Schneider, W. S. Rasband, K. W. Eliceiri, NIH Image to ImageJ: 25 years of image analysis. *Nat. Methods* **9**, 671–675 (2012).
89. S. Bolte, F. P. Cordelières, A guided tour into subcellular colocalization analysis in light microscopy. *J. Microsc.* **224**, 213–232 (2006).
90. N. R. Markham, M. Zuker, UNAFold: Software for nucleic acid folding and hybridization. *Methods Mol. Biol.* **453**, 3–31 (2008).
91. S. W. Taylor, D. B. Chase, M. H. Emptage, M. J. Nelson, J. H. Waite, Ferric ion complexes of a DOPA-containing adhesive protein from *Mytilus edulis*. *Inorg. Chem.* **35**, 7572–7577 (1996).
92. D. S. Hwang, H. Zeng, A. Masic, M. J. Harrington, J. N. Israelachvili, J. H. Waite, Protein- and metal-dependent interactions of a prominent protein in mussel adhesive plaques. *J. Biol. Chem.* **285**, 25850–25858 (2010).
93. H. Zeng, D. S. Hwang, J. N. Israelachvili, J. H. Waite, Strong reversible Fe³⁺-mediated bridging between dopa-containing protein films in water. *Proc. Natl. Acad. Sci. U.S.A.* **107**, 12850–12853 (2010).

Acknowledgments: We wish to thank M. J. Ladu and D. Balu for training in brain slices staining and imaging, as well as suggestions and discussions to improve this project. We thank H. Ihms for contributions and efforts in the iron DNAzyme selections. We thank S. McMasters of the University of Illinois School of Chemical Sciences Cell Media Facility for assistance with cell culturing, the Institute for Genomic Biology Core Facility and Center for Biomedical Research Support Microscopy and Imaging Facility at the University of Texas at Austin (RRID no. SCR_021756) for assistance with confocal microscopy, and the Roy J. Carver Biotechnology for assistance with flow cytometry and use of their fluorescence microplate reader. We thank Z. You and X. Shi for discussion and suggestions for the statistical analysis. We would also like to thank the following individuals for fruitful discussions and support over the course of this project: C. McGhee, K. Hwang, N. S. R. Satyavolu, K. Harden, C. Reed, Q. "Sherry" Tian, Z. Wu, W. Wang, H. Fan, Z. Chen, T. Kehl-Fie, and A. S. Peinetti. **Funding:** This work was supported by the National Institutes of Health (R35GM141931 to Y.L. and R01GM114588 to L.M.M.), the Alzheimer's Association (AARG-NTF-22-926483 to Y.L.), and the Robert A. Welch Foundation (grant F-0020 to Y.L.). **Author contributions:** S.-F.T. and K.N. performed the in vitro selection experiments. S.-F.T. obtained iron-specific DNAzymes and performed the sequence analysis and DNAzymes characterizations. P.W. and R.J.L. designed the fluorescent sensors and performed the in vitro fluorescent assays. Y.W., Z.Ya., G.T.P., and J.V.S. involved in sensor characterization and validation. S.H., Y.W., R.J.L., W.G., and X.S. performed the intracellular imaging. Y.W. performed mouse brain tissue detection and analyzed imaging data. Z.Yu and L.M.M. provided the brain slices. Y.L. proposed and obtained funding for the work. Y.W., S.-F.T., R.J.L., and Y.L. wrote the manuscript with input from all authors. **Competing interests:** The authors declare that they have no competing interests. **Data and materials availability:** All data needed to evaluate the conclusions in the paper are present in the paper and/or the Supplementary Materials.

Submitted 6 September 2022

Accepted 20 March 2023

Published 19 April 2023

10.1126/sciadv.ade7622